

GPU Accelerated 3-D Modeling and Simulation of a Blended Kinetic Impact and Nuclear Subsurface Explosion

Brian Kaplinger, Pavithra Premaratne, Christian Setzer, and Bong Wie^a

^a*Asteroid Deflection Research Center, 1200 Howe Hall, Iowa State University, Ames, IA, 50011, United States, +1 515-294-3124, bdkaplin@iastate.edu, pdp@iastate.edu, csetzer@iastate.edu, bongwie@iastate.edu*

Abstract

This paper develops a modeling and simulation framework for determining mission effectiveness of a two-body Hypervelocity Asteroid Intercept Vehicle (HAIV). This HAIV concept has been being developed to overcome key difficulties in coupling energy from nuclear explosives to an asteroid target at high relative velocities of 5 - 30 km/s. It does so by blending the concepts of a kinetic impactor and a nuclear subsurface explosion to create successive impacts that mimic the behavior of a buried explosive, increasing energy coupling by an order of magnitude. To demonstrate this increase in effectiveness, this approach is simulated in a Smoothed Particle Hydrodynamics model adapted for high-speed, low-cost, implementation on Graphics Processing Units.

An improved 3D simulation system is developed that includes improved neighbor finding for parallel calculations. Fidelity to an inhomogeneous, asymmetric target model is increased to allow for better damage prediction and shock localization. Statistical tracking of the resulting fragments is used to determine efficacy for a variety of nominal orbit conditions.

Keywords:

Simulation, Near-Earth Object, Impact, Hydrodynamics, GPU

1. Introduction

While the most likely near-term threat from Near-Earth Objects (NEOs) is that of a low altitude airburst, the expected energy of an event such as Tunguska would be devastating in a highly populated area. Additionally, though the population of catastrophic impactors has been well surveyed, it is estimated that thousands of bodies over 140 m in diameter remain undiscovered [1]. Many methods have been suggested for the mitigation of this threat, but most require substantial lead time in order to be effective. A study by the United States National Research Council suggests that nuclear explosive devices may be the only option for late warning cases [2]. Arguments have been provided in the past that even low nuclear yields exceed the binding energy of most rubble-pile asteroids, and therefore this method would result in fragmentation of the target. Sanchez et al. [3], provided an analytical framework demonstrating that fragmentation at low energy can be an undesirable effect, despite the dispersion along the orbit of the resulting fragments. Previous simulations, however, show that disruption at higher energies may substantially reduce the amount of mass remaining on impact trajectories. This method could be available with as little as 10 days of lead time between intercept and the predicted impact date for an orbit like that of the asteroid Apophis [4, 5].

This paper describes the extension of a modeling and simulation framework for determining mission effectiveness of a two-body Hypervelocity Asteroid Intercept Vehicle (HAIV) [6]. This HAIV concept has been being developed as part of a NASA Innovative Advanced Concepts (NIAC) Phase 1 and 2 studies to overcome key difficulties in coupling energy from nuclear explosives to an asteroid target at high relative velocities of 5 - 30 km/s. It does so by blending the concepts of a kinetic impactor and a nuclear subsurface explosion to create successive impacts that mimic the behavior of a buried explosive, increasing energy coupling by an order of magnitude. This approach would allow us to bypass the impact speed limit of approximately 1.5 km/s for the explosive payload [7] while still not having to rendezvous with the NEO. For late warning time, fuel requirements for a rendezvous mission may be outside of current capabilities, so missions with direct intercept trajectories will be easier to accomplish and more robust to uncertainty. Such missions can be launched to intercept all the way up to the 10-15 day lead time limit [8].

To demonstrate this increase in effectiveness, this approach is simulated in a Smoothed Particle Hydrodynamics (SPH) model adapted for high-speed, low-cost, implementation on Graphics Processing Units (GPU). Initial simulations in [5,9] used a spherical axisymmetric near-Earth object (NEO) model, with the key limitations being the size of the target and a lack of a range of source energy input. With a new computational approach to the hydrodynamic simulations, we efficiently compute results for a 2-D inhomogeneous shape of user-selected characteristics, such as that shown in Figure 1. We also extend the model to general 3-D shapes imported from a surface triangulation, such as the scaled shape model for 433 Eros also shown in Figure 1. This will allow us to address much larger targets with increased resolution and a faster turnaround time, so the influence of more composition parameters can be investigated. An analysis of the sensitivity to the explosive timing is conducted.

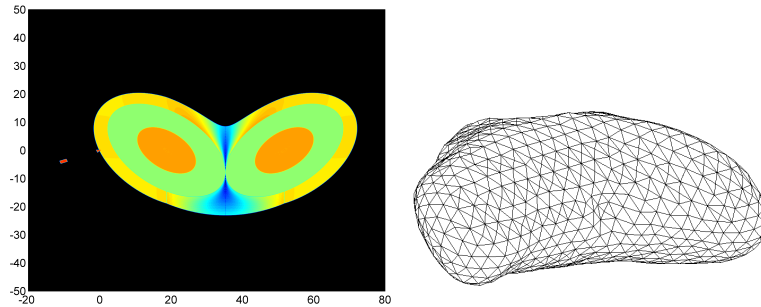


Figure 1: Slice of Contact Binary Model and Triangulated Shape Model for 433 Eros.

A nonlinear orbit solver is presented that calculates an impacting trajectory given boundaries of an (a, e, i) sampling space. This approach increases our understanding of what components of the interplanetary environment affect the likelihood of a NEO being on a collision path with the Earth. New high-throughput neighbor-finding methods are suggested for the particle representation of disrupted NEOs. This approach becomes more effective using the GPU acceleration technology of the current simulation toolkit. In contrast to the Weibull distribution used to seed implicit flaws in brittle materials [5,9], the current simulation set develops a tensor relationship for material characteristics and orientation. This allows for more realistic size and shape generation for NEO fragments by treating damage as a local quantity (cracks) rather than a distributed state variable. One of the key limitations is that most proposed neighbor-finding methods for interpolation rely on complex logic and lists not suitable for efficient GPU implementation. Therefore, the addition of the third dimension makes this problem far more complex. A bin process used in previous SPH research is extended for the GPU computing platform.

Previous work [5,9] showed that a large amount of data can be processed using GPU simulation. Initial work was focused mostly on prediction of relative impacting mass, but disruption at different times along a given orbit can have a large effect on the resulting shape of debris. The proposed approach looks at the fragmentation model to better address how uncertainty in the NEO breakup affects orbital prediction, particularly in the case of variable time-to-impact. This allows for a more clear set of objectives for mission design. Another new result is the availability of representative 3-D fragment distributions for non-spherical bodies. This will improve the trajectory of the desired hypervelocity intercept mission by allowing full degrees of freedom in choosing the approach asymptote.

2. Methods

This section describes the methods used to generate the simulation model. A discussion of the extensions from past work is given, as well as new relationships for the SPH implementation and damage model. The core SPH concepts are discussed in [5], which is built upon a wealth of past SPH literature and programmed on the GPU using the CUDA framework [10].

2.1. Adaptive Smoothed Particle Hydrodynamics

Since the hypervelocity impact and explosive simulations rely heavily on energy transmission through shocks, the current simulation framework uses Adaptive Smoothed Particle Hydrodynamics (ASPH) to mitigate some of the computational and fidelity issues that arise in more complex simulations. This approach is explained clearly by Owen et al. [11], the implemented details of which are repeated here. A concise explanation of the differences from “standard” SPH can be found in [12]. SPH uses a kernel function that acts on a normalized position space. This kernel, $W(\nu)$ is a function of the normalized distance vector $\nu = r/h$, where r is the physical distance vector, and h is the isotropic smoothing length. To add a direction sense to ellipsoidal nodes, ASPH uses a symmetric, positive definite linear transformation G such that $\nu = Gr$. Then, the kernel derivative becomes:

$$\nabla W(\nu) = G \frac{\nu}{|\nu|} \frac{\partial W}{\partial \nu} \quad (1)$$

Given a matrix representation of the tensor G , the entries are evolved by:

$$\frac{DG}{Dt} = \frac{DR}{Dt}G - G\sigma \quad (2)$$

where $\sigma_{ij} = \partial v_i / \partial x_j$ is the deformation tensor. This can be easily obtained from the strain rate tensor and rotation rate tensor used for the general SPH implementation. R is an infinitesimal rotation of the smoothing kernel. It is well defined at the current time by noting that it must be antisymmetric and that the resulting offdiagonal elements of DG/Dt must be symmetric. A description of a process to calculate these intermediate terms is given in [11].

A smoothing process for the tensor G is implemented after many time steps, as suggested in [12]. This is done as a weighted average over the neighboring values to generate the new smoothing tensor G' by

$$G' = |G| |g_i| g_i \quad (3)$$

where

$$g_i = \frac{\sum_j G_j^{-1} W_{ij}}{\sum_j W_{ij}} \quad (4)$$

To mitigate spurious shear viscosity that is introduced by the artificial viscosity Π_{ij} , we modify this viscosity calculation using the Balsara correction [13] as follows:

$$\tilde{\Pi}_{ij} = \frac{1}{2}(f_i + f_j)\Pi_{ij} \quad (5)$$

where

$$f_i = \frac{|\nabla \cdot v_i|}{|\nabla \cdot v_i| + |\nabla \times v_i| + \delta c_i / h_i} \quad (6)$$

and c is the local sound speed and δ is a small number chosen to prevent divergence.

2.2. Tensor Damage Model

In the initial SPH model for comparison, the behavior of the core material under high stress is governed by the activation of implicit flaws. These flaws are seeded in the representation particles using a Weibull distribution with a coefficient of around 4.2E23 and an exponent between 6.2-9.5. Using a range of distribution exponents and strength properties allows us to examine the behavior of the core material with varying brittleness and material cohesion. This turns out to be very important for this contact binary system, as strong core material absorbs energy from the disruption shock and can result in large remaining chunks of material. Smoothing lengths are chosen to allow for resolution of between 1 cm and 5 cm, which results in a hydrodynamic system of between 800,000 and 6,000,000 nodes. This system is scaled to be an ideal size for the GPU simulation programs developed at the Iowa State Asteroid Deflection Research Center (ADRC), maximizing both computational efficiency and simulation turnaround time.

For this comparison, a damage model using a tensor variable was implemented. The details are the same as those used in the Spheral code, developed by Mike Owen at the Lawrence Livermore National Laboratory. We use a tensor damage variable defined per node $D^{\alpha\beta}$ in order to support directionality in the damage evolution. Cracks are allowed to open up in response to strain aligned perpendicularly to that direction, there is substantially reduced crack growth in orthogonal directions to the strain. The tensor strain, $\sigma^{\alpha\beta}$ used is the “pseudo plastic strain” of SolidSpheral, due to Mike Owen, which evolves in time as

$$\frac{D\sigma_i^{\alpha\beta}}{Dt} = \frac{1}{G_s} \frac{DS_i^{\alpha\beta}}{Dt} \quad (7)$$

This is decomposed into a set of eigenvalues, σ^ν , and eigenvectors, $\Lambda^{\alpha\nu}$, from which the directional scalar damage, Δ^ν is the magnitude of the ν -th column of $D^{\alpha\gamma}\Lambda^{\gamma\beta}$. The maximum damage allowed to accumulate in a volume, similar to the formulation in [5,9] but allowing for directionality, is:

$$D^{\max} = \max\left(\frac{n_i}{n_i^{\text{tot}}}, \Delta_i^\nu\right) \quad (8)$$

where n_i is the number of active flaws ($\epsilon > \epsilon^{\text{act}}$) and n^{tot} is the total number of flaws assigned to a particle, which can vary widely, but is always at least one. These directional damages can then be time evolved using representative scalar evolution laws [9,14].

2.3. Neighbor Finding Implementation

In order to speed up neighbor-finding calculations with the increased dimensionality, a tree data structure was used to superimpose a sparse physical grid on the data. This implementation is similar to several approaches used to simulate local gravity interactions in astrophysical simulations. First, the coordinate arrays are sorted and then an inverse map for the particle IDs into the sorted array is defined as in [15,16]. Then, a partitioning of the sorted space is defined so that each grid box represents a nearly equal number of particles, and that all the particles in neighboring grid locations are greater than the desired maximum of particle neighbors. This is a hard limit due to memory structure on the GPU data representation.

Each bin is assigned a list of particles in it. Then, a neighbor search for a particle limits itself to the particles in the nearby grid bins. With a well-defined number of particles per bin, this results in an implementation that scales linearly with number of particles. The main limitation is in the assignment of particle IDs to the bin and in the storage requirements for this connectivity information. However, storage added is small compared to the storage of neighbor IDs for each particle, and the sort and assignment can be done in parallel on the GPU. The power of this approach lies in how it scales with increased number of SPH interpolants. In addition to scaling superlinearly (compared to quadratic brute force calculations), the present approach uses the Thrust library to sort the position components of the particles in parallel. This eliminates a series of memory transfers with the host and keeps all data on the GPUs.

A subsequent group of GPU kernels establish pointers to the limits on the sorted array for which candidate neighbor particles may belong. This reduces the neighbor finding to an integer union calculation, which can be conducted as a logical (true/false) operation. Comparing the position of the sorted particle IDs with the limits allows for a simple yes/no decision on whether a proposed neighbor could be within the support of the interpolation function. Figure 2 gives a depiction of this process for each computing thread. Figure 3 shows the improvements of the present model over in-place neighbor calculations (also on the GPU). While dimensionality affects the speed-up, there are still substantial gains made over past implementations.

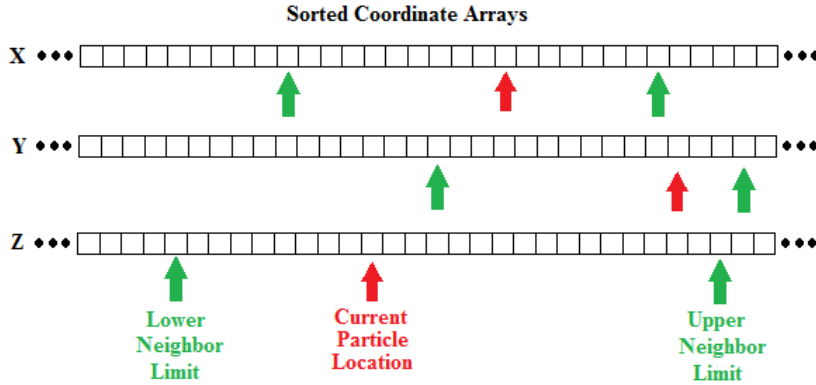


Figure 2: Description of Sorted Neighbor Kernel Process.

2.4. Grid Generation

An automatic grid generation for the SPH input conditions has been developed. Currently, the modeling program requires a function for a piece-wise defined surface $z = F_i(x, y)$. The pieces should not overlap, and the surfaces for $z > 0$ and $z < 0$ can be distinct. A uniform grid of points (x, y) are created and the initial conditions for the optimization are $(x_0, y_0, z_0) = (x, y, F(x, y))$. Then, updates to these positions are made to satisfy the local problem

$$\min \sum_j (r_{ij} - d)^2 \text{ subject to } z_i = F(x_i, y_i) \quad (9)$$

where d is the specified desired optimal separation, the sum is over the immediate neighbors, and r_{ij} is the distance between points i and j . Note that this problem is solved independently for each point i . An iterative update scheme is converged until the boundary particles are seeded. Then, a uniform grid of interior particles is initialized. The positions of these points are similarly updated using an unconstrained problem

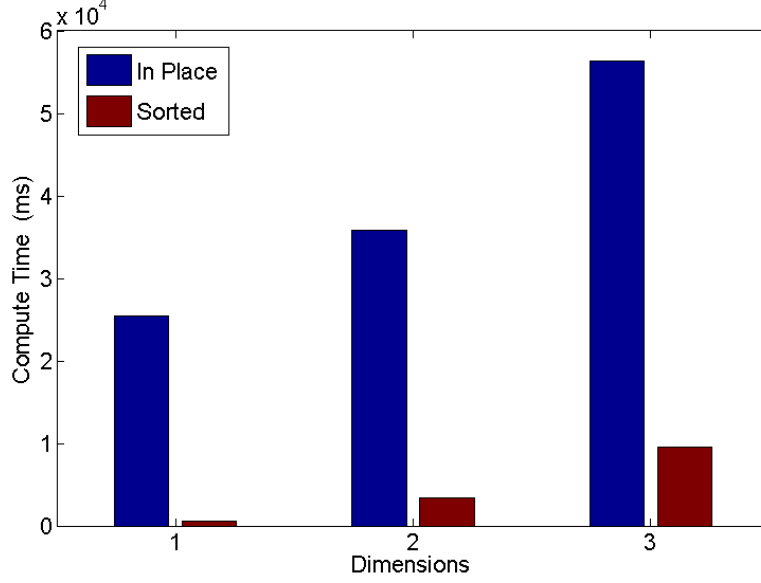


Figure 3: Neighbor Search Cost.

$$\min \sum_j L_{ij} \quad (10)$$

where L_{ij} is the Lennard-Jones potential in terms of our desired spacing, d , and a potential well magnitude ϵ [17]:

$$L_{ij} = \epsilon \left[\left(\frac{d}{r_{ij}} \right)^{12} - 2 \left(\frac{d}{r_{ij}} \right)^6 \right] \quad (11)$$

2.5. Impacting Orbit Solver

The orbital parameters for the nominal trajectory are sampled from a (a, e, i) space that represents the distribution of known NEOs, as shown in Figure 4. This is done using inverse transform sampling, in which a random number is mapped to the integral of the cumulative density function for each of these three parameters. Given a , e , i , and the impact date, we have all of the information needed to pin down an impacting orbit. If we assume that the orbit passes through the center of the Earth, then we have x_E , y_E , and z_E , which are the Cartesian coordinates for the Earth's center of mass at that epoch, which coincide with a point on the desired orbit.

Given a , e , and $r = \sqrt{x_E^2 + y_E^2 + z_E^2}$, the specific angular momentum is calculated as $h = \sqrt{\mu a(1 - e^2)}$ [18,19]. Then, the true anomaly, θ and velocity magnitude, v , are calculated using the orbit equation and the vis-viva equation:

$$r = \frac{h^2}{\mu} \frac{1}{1 + e \cos \theta}; \quad \frac{v^2}{2} - \frac{\mu}{r} = -\frac{\mu}{2a} \quad (12)$$

We can also calculate the radial velocity, v_r , as

$$v_r = \frac{\mu}{h} e \sin \theta \quad (13)$$

which gives us all the needed scalars to solve the following set of nonlinear equations for the velocity components v_x , v_y , and v_z , resulting in the desired state vector:

$$\begin{aligned} f_1(v_x, v_y, v_z) &= 0 = xv_y - yv_x - h \cos i \\ f_2(v_x, v_y, v_z) &= 0 = xv_x + yv_y + zv_z - rv_r \\ f_3(v_x, v_y, v_z) &= 0 = \sqrt{v_x^2 + v_y^2 + v_z^2} - v \end{aligned} \quad (14)$$

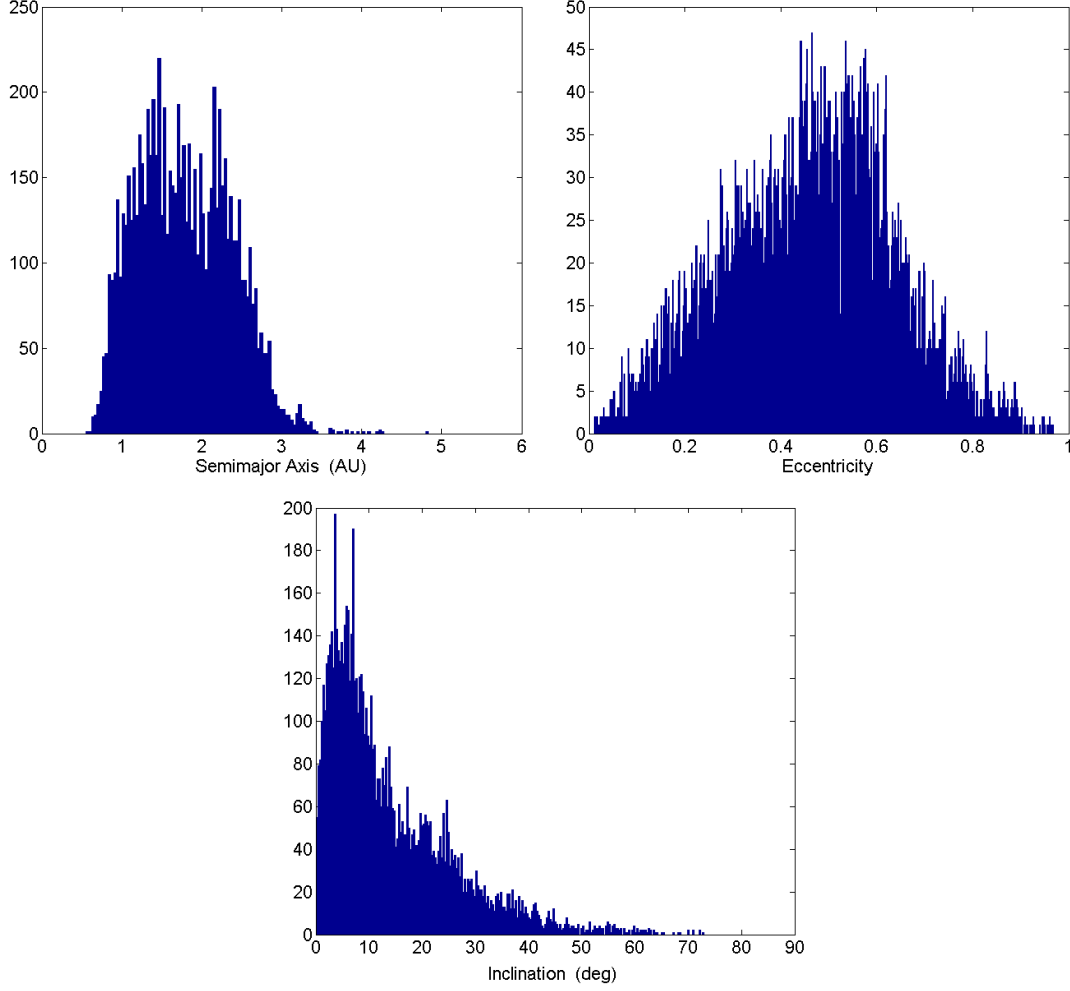


Figure 4: Histograms of Known NEO Population.

2.6. Fragmented System Estimation

Statistics representing the fragmented system are collected and stored as cumulative density functions for the needed variables, similar to those shown in Figure 5. A representative fragment system of 10,000 to 100,000 fragments is created from these statistics using inverse transform sampling. The debris cloud is given global coordinates in a Local-Vertical-Local-Horizontal (LVLH) reference frame about the center of mass, as shown in Figure 6. Since the hydrodynamic model is axisymmetric, and has a definite direction of maximum momentum along the axis of symmetry, a desired deflection direction must be chosen. These are then integrated to predict an ephemeris for a 48 hour period surrounding the nominal time of impact. Since the LVLH reference frame is computationally beneficial for self-gravity and collision modelling among fragments [20], we use the nonlinear relative equations of motion for this frame to govern fragment trajectories [4,18,19,20]:

$$\ddot{x}_i = 2\dot{\theta} \left(\dot{y}_i - \frac{\dot{r}_c}{r_c} y_i \right) + \dot{\theta}^2 x_i + \frac{\mu}{r_c^2} - \frac{\mu}{r_d^3} (r_c + x_i) + \frac{\mu_E}{r_{Ei}^3} (x_E - x_i) + F_i^x \quad (15)$$

$$\ddot{y}_i = -2\dot{\theta} \left(\dot{x}_i + \frac{\dot{r}_c}{r_c} x_i \right) + \dot{\theta}^2 y_i - \frac{\mu}{r_d^3} + \frac{\mu_E}{r_{Ei}^3} (y_E - y_i) + F_i^y \quad (16)$$

$$\ddot{z}_i = -\frac{\mu}{r_d^3} z_i + \frac{\mu_E}{r_{Ei}^3} (z_E - z_i) + F_i^z \quad (17)$$

where x , y , z , r_c , and θ are defined as shown in Figure 6, r_d is the length of the relative coordinate vector, μ and μ_E are gravitational parameters for the sun and the Earth, r_{Ei} is the distance from each fragment to Earth, and (F^x, F^y, F^z) are the combined acceleration components due to 3rd body gravitational terms (solar system major body model [4]), self gravity, and collision corrections. The threading structure for computing the values for self

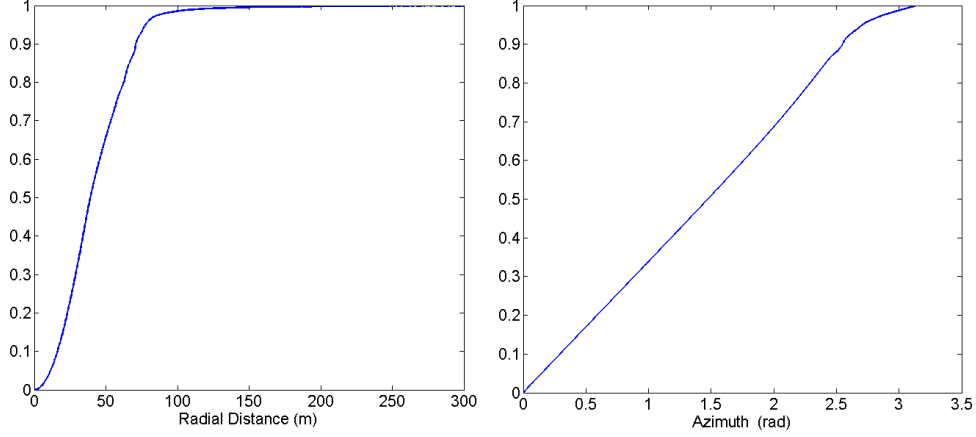


Figure 5: Cumulative Density Functions for Disrupted Asteroid.

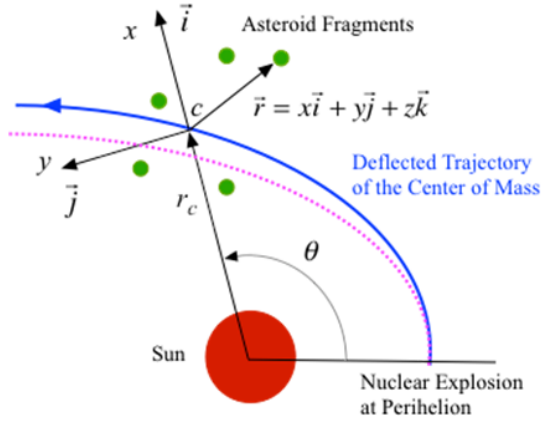


Figure 6: Rotating Local-Vertical-Local-Horizontal (LVLH) Frame.

gravity terms is described in [20], while collisions are predicted using a Sort-and-Search algorithm [15], resulting in post-collision changes to position and velocity of fragments. An elastic spherical collision model is assumed for the fragments, with a coefficient of restitution of 0.5.

2.7. Uncertainty Analysis

In order to test the response of orbital dispersion with respect to uncertain initial fragment positions and velocities, a Gaussian noise is added to the mapping around the nominal center of mass. A standard deviation of 10% is assumed, resulting in deviations from the hydrodynamic simulations up to $\pm 30\%$. For a given orbit, 1000 random perturbations are integrated to impact, resulting in an average system behavior and a standard deviation representative of the uncertainty due to the initial conditions.

This procedure is completed for a database of 906 orbits chosen to impact at a fixed date. The orbital parameters for the nominal trajectory are sampled from a (a, e, i) space that represents the distribution of known NEOs, as shown in Figure 4. For each chosen deflection direction, the Monte Carlo procedure described above results in a characteristic behavior of a disrupted NEO on the range of orbits tested.

Given a fixed lead time in which to allow the fragmented target to disperse along its orbit, or even a minimal desired lead time, we have a point (or set) at which a desired intercept is achieved. It is clear, however, that not all approach vectors are equal. From a mission design perspective, the approach asymptote affects the transfer orbit, and therefore the cost (or even feasibility) of the mission [8]. For the present study, bounds on the approach asymptote from a mission perspective are not considered. Rather, the direction in which the approach occurs is a deciding factor in the behavior of the fragmenting body. Past work has shown that there is a clear bias towards dispersion along this vector for most of the tested hydrodynamic simulations [9].

A simple differential optimization routine is applied to this vector for each of the sampled impacting orbits. There are two degrees of freedoms for each of these problems. The optimal pointing direction will be something of interest

in short warning scenarios, since a drastic difference in the dispersion patterns can occur. For some of the orbits, a grid search of the approach asymptotes was done to quantify the range of impacting mass ratios.

3. Results and Discussion

This section describes the results of the present research effort. A description of the targets used for 2D and 3D analysis is given. Sensitivity of the resulting energy transfer from explosion to both timing and payload position is demonstrated. Finally, a comparison of the proposed HAIV concept to a surface burst is simulated.

3.1. HAIV System Targets

Initial demonstration of the two body HAIV concept used spherical spacecraft dummy payloads to hit an inhomogeneous target with a diameter of 54 m. This method was directly compared to a single explosion on contact with the surface. The current asymmetric target consists of a contact binary system with a rubble pile exterior. With binary systems comprising about 16% of the known NEA population [21], an impactor mission faces an approximately 1 in 6 chance that the target it approaches will be a binary system. This is a characteristic that will be unable to be predicted ahead of time without radar observation, in the case of systems with close secondaries. It has been suggested that many irregularly shaped asteroids with unusual spin states could be contact binary (or multiple) systems. These types of systems would exhibit some of the same characteristics as monolithic rocks and as rubble piles [22]. Further, those asteroids identified as rubble piles could have large solid components beneath their regolith.

The two cores of the model system are elliptical, with major and minor axes of 50 and 30 meters, respectively. These cores are given material properties similar to granite using a linear elastic-plastic strength model, and are canted by 45 degrees relative to the horizontal. There is a vertical line of symmetry, so the cores are mirror images of one another. A rubble regolith extends 2 meters in depth vertically above each core, and is packed along lines of constant potential around the body, resulting in a maximum regolith depth of 14 meters. These properties result in exterior dimensions of the target being approximately 76 x 42 meters, as shown in Figure 1. The inner half of each core has an initial bulk density of 2630 kg/m³, while the outer portion of the core is more porous material with an average bulk density of 1910 kg/m³. A linear model for material strength is used in this target with a yield strength of 14.6 MPa and a shear modulus of 35 MPa, resulting in a more granulated fragmentation and slower dispersion velocities. Real asteroid targets are expected to fall within the two extremes discussed earlier, with variances for composition, distribution of mass, and orientation.

The overall velocity statistics for this case, which are the governing variables behind successful disruption, are similar to those for the cylindrical case. The histogram for radial dispersion velocities of the fractured particles can be seen in Figure 7. There is a mean dispersion velocity for the HAIV case of almost 350 m/s.

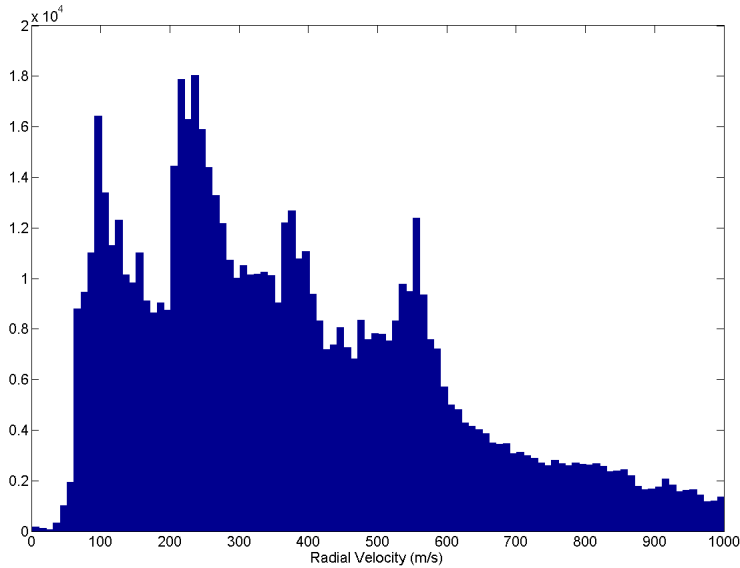


Figure 7: Radial Dispersion Velocity Histogram for HAIV Concept.

The travel of the explosive shock can be seen in Figure 8. This process dissipates some energy due to interactions with the rebounding shock front. In the center area of deeper regolith, the seeding process naturally results in a much

more porous material, absorbing energy from the shock. The new damage model allows for better tracking of crack propagation. Upon reaching the second core at the far side, some large chunks escape the disruption process in some cases (even with lower material strengths). A final hydrodynamic state can be seen in Figure 9.

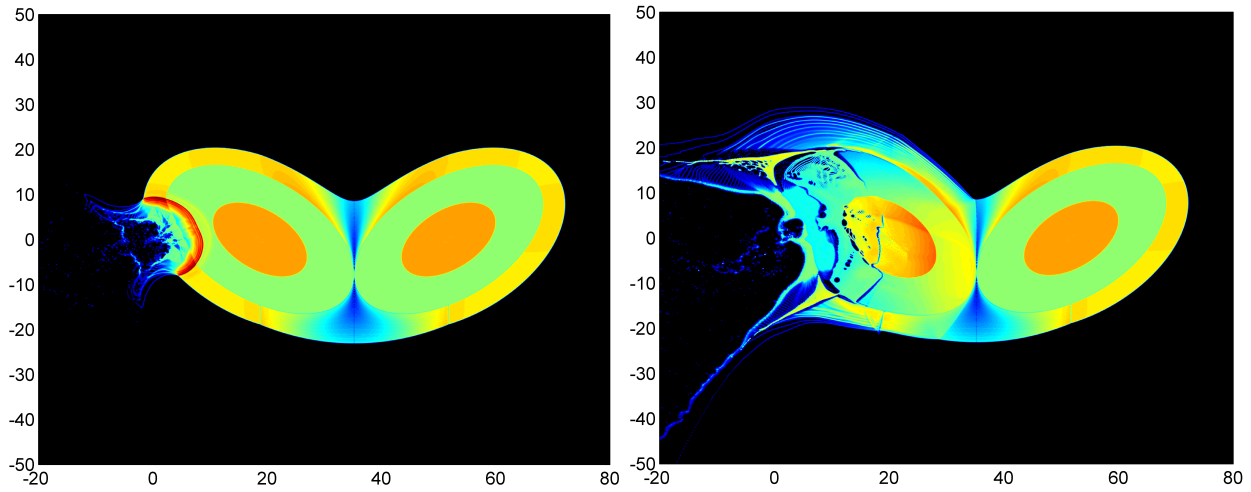


Figure 8: Asymmetric Shock Behavior.

There remains a high risk for this target of single largest chunks on the order of tens of meters. However, this material is highly stressed due to velocity gradients, and may be ripped apart in further time. The large velocity gradients and the location of the slowest debris can be observed in Figure 9. Further, these large chunks are still imparted substantial velocities from the blast approximately 10-20 m/s, and have sufficient energy to disperse from the nominal impacting trajectory over tens of days.

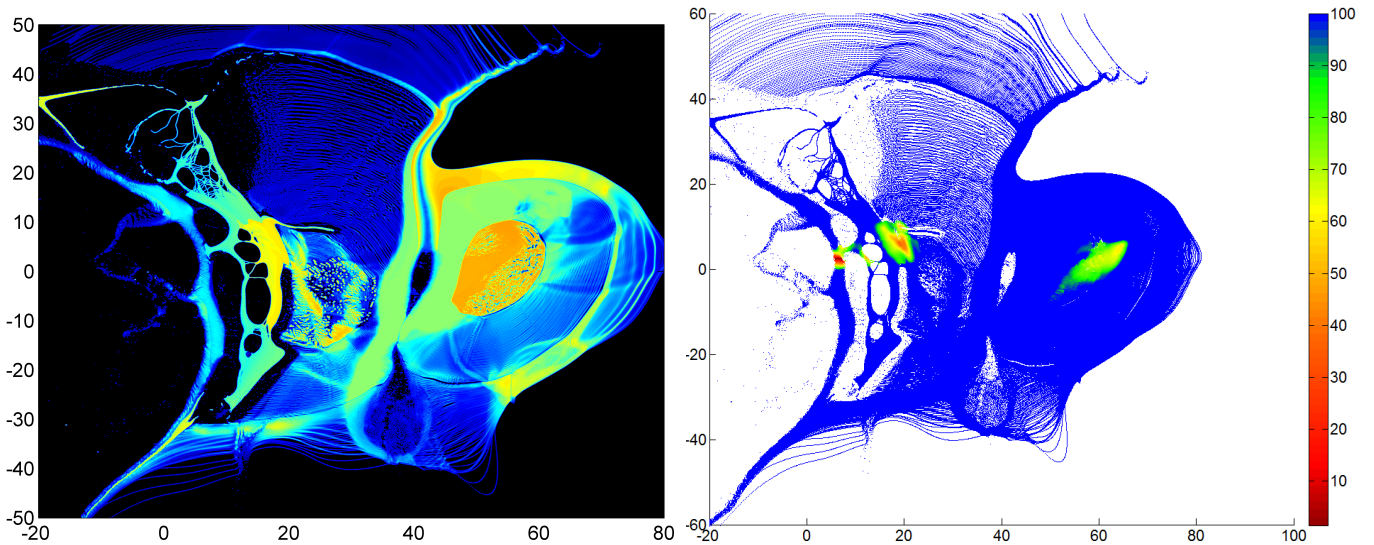


Figure 9: Final Disruption of NEO Target and Location of Slowest Moving Debris.

3.2. 2D Blast Sensitivity

A series of sensitivity and validation studies using a 2D SPH algorithm have been conducted in order to identify mission critical information. The tests incorporated a spacecraft model with a leading impactor and a following nuclear payload. A 70 m wide asteroid was set as the target and the studies below were performed to determine a better location to detonate the payload. The first task was to study payload detonation in multiple locations of the crater. Once the impactor creates a crater, the payload was guided to different locations of the crater to qualitatively identify the magnitude of the damage caused by the nuclear detonation. The second task was payload detonation in a series of locations between above the surface and the bottom of the crater. Detonations were conducted below and under the surface level to observe damage. The final qualitative study was correlation between the crater size and

the damage from the nuclear detonation. Particle dispersion and fragmentation were analyzed after detonating the nuclear payload in the bottom of the crater. Different sizes (width) of intermediate crater formation were created by adjusting the distance between the impactor and the payload.

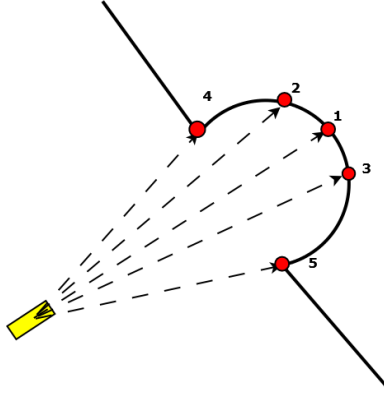


Figure 10: Test Locations for Payload Placement Sensitivity Analysis.

We simulated the following scenarios depicted in Figure 10. The nuclear payload should be detonated just before it starts its deformation after contacting the surface. A 50 kt energy source was used. Velocity magnitude of both impactor and the payload is 10 km/s at all times. The direction and the velocity magnitude of the impactor will not change in this case. The nuclear payload was detonated before it starts to deform after contacting the surface. All the simulations were run for approximately 6 ms simulation time.

The images in Figures 11 and 12 show the progression of the collision and explosion through time. The payload impacts the bottom of the crater, at which point the width of the crater is 6.4 m. Depth of the crater is 5.0 m. A shock propagation can be observed along with a destabilization of the surface layers and a layer near the core. In the final intermediate stage, more surface layers shows a shredding effect along with a density change in the middle layers. At test points 2 and 3, the first image shows the front of the payload has begun to deform. This image was taken right before the payload was detonated. At 200 time steps, a smaller shock has started to propagate adjacent to the larger one which suggests that particles with high kinetic energy (from the payload) have taken some time to reach with that specific point. At the final intermediate stage, the smaller shock has merged into the larger one. More particles from the surface layer have been dispersed with the presence of a peeling effect compared to location 1. Location 2 and 3 shows a symmetry in the results. This symmetry can be observed by comparing the 2 figures of intermediate steps after the payload detonation.

For test points 4 and 5, the payload impacts the elevation of the ground at the top end of the crater. These locations also show the same kind of symmetry in results. The location of the initial crater seemed to have moved through the particle distribution relative to the location of the explosion. Particle dispersion seems to be a lot less in these scenarios compared to other scenarios in the same intermediate crater formation time scale.

We also conducted simulations to identify which configuration of impactor-payload is better for a mission. The test should be conducted with an initial distance between a payload and impactor 40 m. Figure 13 shows possible locations of impact. The simulations were run for approximately 0.012 s. The first location is the nominal case of impact at the bottom of the crater formed by the primary impactor. For case 2, the payload was detonated as the front of the payload intersected with the initial surface height. This location is slightly below the surface at this time. Distance from crater bottom to payload is approximately 7 meters. The third test point was at $x = -2$. This point is located slightly above the current surface line, and the bottom of the crater from the payload is about 9.5 m. The final case was an initial explosion location of $x = -9.0$. This case was run for about 10 ms. Distance from bottom of the crater to payload is approximately 15.75 m. Before and after images of these cases are shown in Figure 14.

3.3. Sensitivity to Orbital Parameters

In order to address the effectiveness of different fragmentation methods, we compare the mass remaining on impacting trajectories (including the uncertainty from the Monte Carlo process) against other methods for each orbit. On average across the orbits tested, the impacting mass was 10% higher for the solid target compared to the rubble target for deflections in the radial direction. Estimates like this will eventually allow for tabular look-up of performance for various methods without direct computation. It was also found that impacting mass for the solid target was 20% higher than the rubble target in the transverse direction.

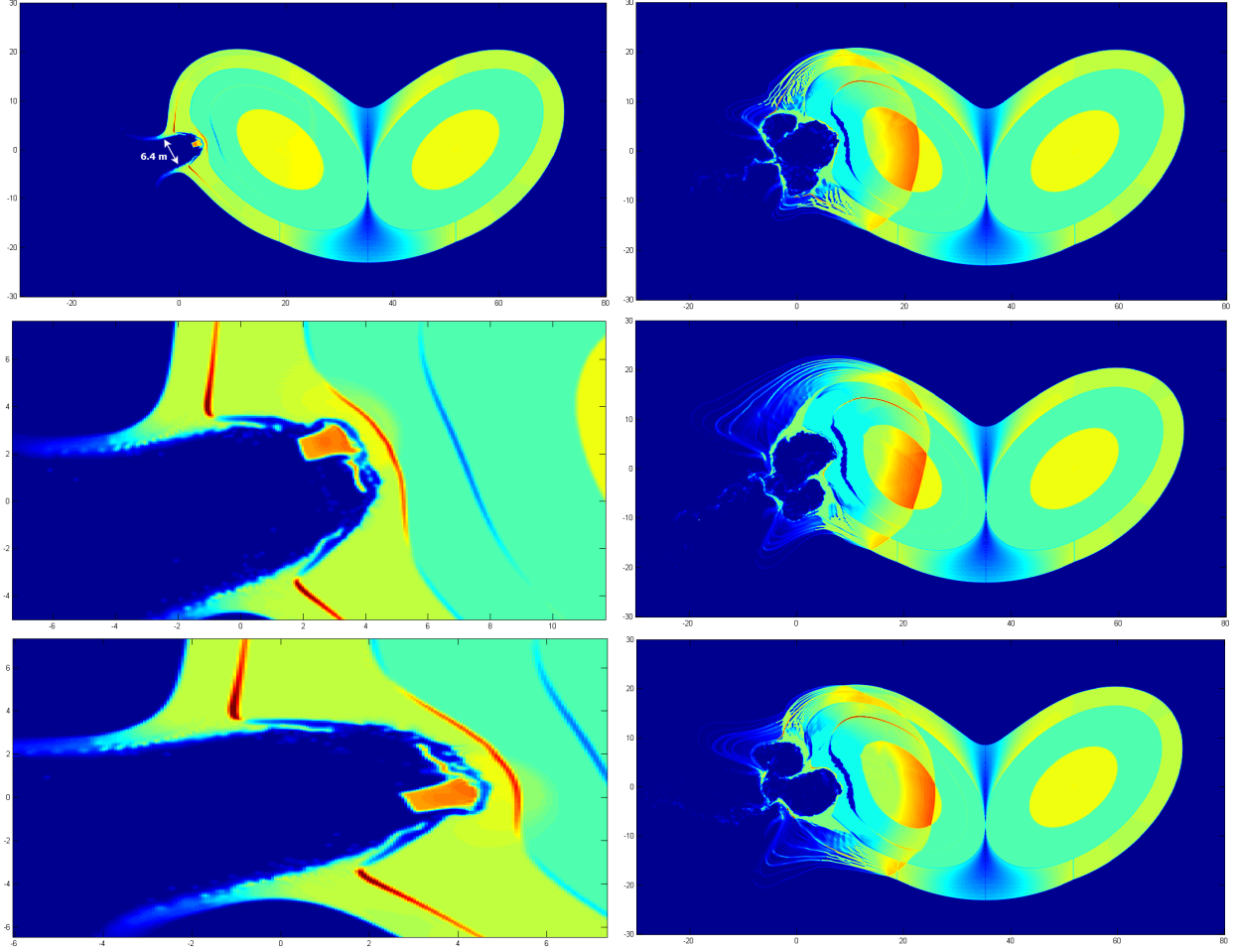


Figure 11: Disruption Behavior for Test Points 1, 2, and 3.

No strong correlation was found for the semimajor axis or eccentricity of the NEO orbit with only 15 days of lead time, however, deflections on orbits with high inclination were more effective, as shown in Figure 15 for the surface blast case.

3.4. Comparison of Surface Blast and HAIIV Concept

Ejecta velocities for the dynamic surface burst (at 6.1 km/s) were within the 10% assumed noise range compared to a static buried explosive. Thus, an emphasis might be placed on hypervelocity intercept and guidance technology rather than a rendezvous mission. One possible interceptor design includes an aluminum impactor followed by an explosive. With both interceptors impacting at 6.1 km/s, the resulting ejecta speed is on average 25% higher than the single surface blast, with a standard deviation of 5.3%. Figure 16 shows the relative velocities for these cases, which results in 20% lower impacting mass on most orbits tested.

3.5. Optimal Mission Results

The present simulation package has the advantage of being able to handle millions of decoupled optimization problems in parallel to one another. Thus, the generation of data outpaces the capability for displaying it in the present work. However, sample results are shown for a nominal impacting trajectory with a lead time of 15 days. Figure 17 shows the cost function contours for approach asymptotes of a sample mission. This impacting trajectory has a semimajor axis of 0.968, an eccentricity of 0.0242, and an inclination of 7.309 degrees.

It is clear for this case that, not only do local optimal solutions exist, but that there are specific conditions which should be avoided. However, this was not the case for all of the virtual impacting trajectories. This fact was especially true for orbits of high eccentricity (> 20 degrees), which had many local minimums, and a wider range of effective dispersion options. Deeper cost function wells existed for these cases, though the geometry was more complicated than the lower inclination case, as shown. The contours are colored according to the base 10 logarithm of the resulting

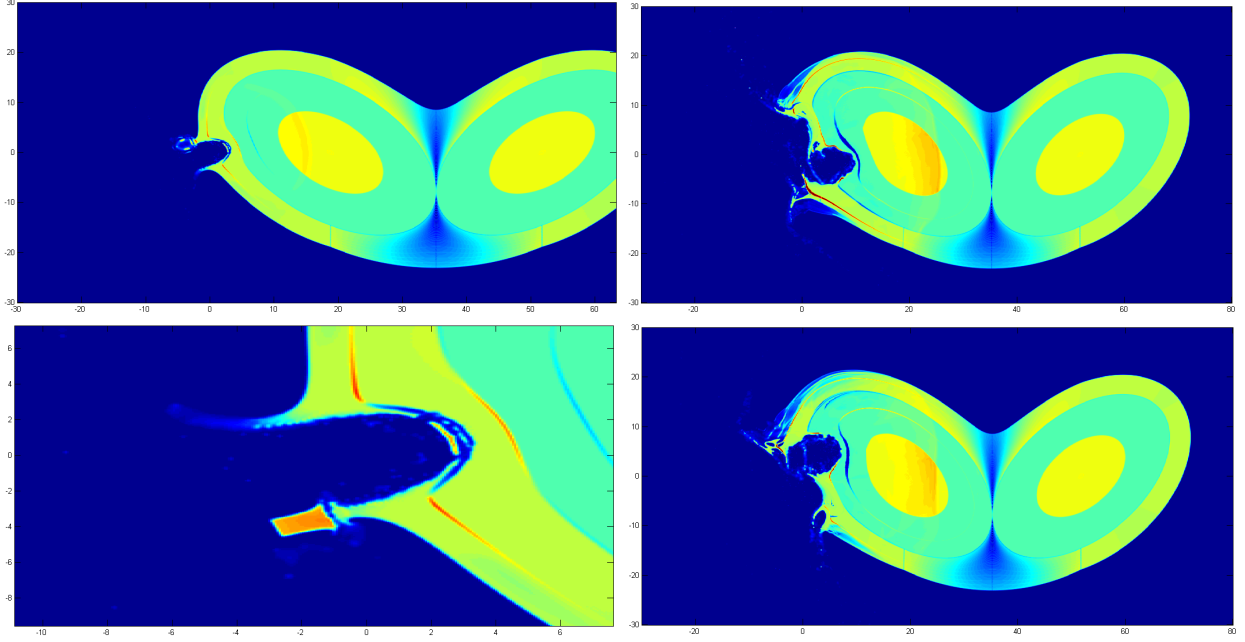


Figure 12: Disruption Behavior for Test Points 4 and 5.

impact probability, showing a range of orders of magnitude. No clear result for the optimal direction for all cases was established. In the sample case, the conditions to be avoided were a perturbation normal to the plane of the orbit. The optimal directions in this case are near parallel to the velocity direction. The vectors forming the solutions of the tested orbits were uniformly distributed, which may be indicative of the lower lead time mission.

As discussed in [8], some approach asymptotes are critical for interception with a single launch. Therefore, future work should address the coupled problem of mission feasibility and mission effectiveness. This will likely place stricter limits on the available lead times and the payload mass deliverable to the target.

4. Conclusions

The present SPH hydrocode suggests that a dynamic model of a hypervelocity surface burst yields results similar in spatial and temporal distribution at Earth impact to a static subsurface explosion. This gives additional launch windows for mission design, limits the fuel needed for a rendezvous burn, and avoids the need to bury the explosive payload. Additionally, the dynamic model should better predict system behavior when addressing high velocity penetrator architectures. The primary mechanism for this improvement is to use impactor momentum to couple

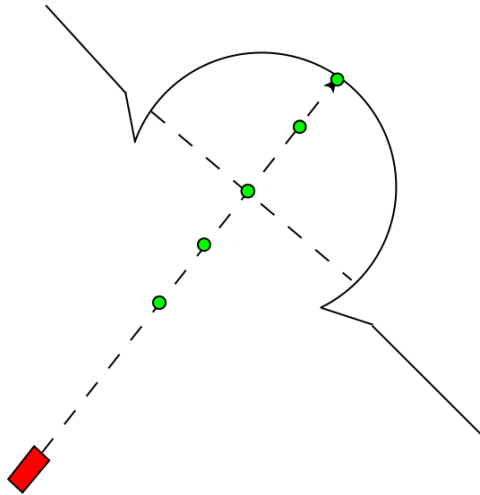


Figure 13: Test Point Locations for Payload Timing Analysis.

energy into the surface material. Since impact at over 6 km/s is not survivable by current explosive system technology, this naive approach is not a viable option. However, the proposed HAIV concept offers similar promise. This might give an option for realistically determining the limits of such a system for asteroid deflection missions. NEO orbital parameters such as semimajor axis and eccentricity were not found to be important for these time scale, but it was found that inclination was important in determining effectiveness of any given method.

All methods of disruption using a 100 kt nuclear energy source were quite effective for 100 m diameter targets for 15 days lead time, regardless of the orbit considered. The existing ADRC models of a hypervelocity impact fragmentation of an NEO were extended and applied to a 3D inhomogeneous asteroid model with randomly generated sections and generic material parameters. It is clear from the discrepancy in dispersion speed for the 76 m asymmetric target that the proposed HAIV concept is successful in reducing the mass remaining on impacting trajectories over a simple contact burst. Future work should consider larger bodies, a range of source energies, and lead times specific to the available mission time for a given orbit.

New HPC technology utilizing GPU acceleration has resulted in orders of magnitude improvement in computational ability. Speedup of the GPU accelerated model compared to serial execution for the both target models has been demonstrated. While the 330,000 particles of the penetrator target are limited mostly by communication bandwidth, the 3.1 million particles in the standoff model are limited by computational speed and memory bandwidth for the threads on the GPU. A substantial speedup improvement, from 53x to 358x, is observed. New high-throughput neighbor-finding methods were suggested, using the GPU acceleration technology of the current simulation toolkit. The current simulation set develops a tensor relationship for material characteristics and orientation. This allows for more realistic size and shape generation for NEO fragments by treating damage as a local quantity (cracks) rather than a distributed state variable. GPU acceleration of the 3D model is up to 200x on a single workstation, continuing a trend of increasing computational complexity while also increasing efficiency. This approach allows us to compute a range of values rather than monolithic single simulations, and is incredibly important for the orbital analysis.

This shows single node computational performance on the same order as a moderate cluster. The ability to run multiple cases to address statistical system behavior results in simulation being integrated into overall mission design. Mission effectiveness can be estimated in advance of a need for mission design, allowing new architectures and interchangeable components for a universal deflection plan. This technology provides a useful reduction in time-to-solution comparable to 30 similar CPU-only nodes (which would cost \$4,000 each) in a \$14,000 form factor, showing a 8.6x improvement in cost-adjusted performance. Since a large amount of data can be processed using GPU simulation, this work confirms that disruption at different times along a given orbit can have a large effect on the resulting shape of debris. This allows for a more clear set of objectives for mission design. Another new result is the availability of representative 3D fragment distributions. This will improve the trajectory of the desired hypervelocity intercept mission by allowing full degrees of freedom in choosing the approach asymptote.

References

- [1] M. Boslough, "Airburst warning and response," *2nd IAA Planetary Defense Conference*, Bucharest, Romania, May 9-12, 2011.
- [2] Committee to Review Near-Earth Object Surveys and Hazard Mitigation Strategies, *Defending Planet Earth: Near-Earth Object Surveys and Hazard Mitigation Strategies*, National Research Council, 2010.
- [3] J. Sanchez, M. Vasile, G. Radice, "On the consequences of a fragmentation due to a NEO mitigation strategy," IAC-08-C1.3.10, *59th International Astronautical Congress*, Glasgow, United Kingdom, September 29-October 3, 2008.
- [4] B. Kaplinger, B. Wie, and D. Dearborn, "Earth-Impact Modeling and Analysis of a Near-Earth Object Fragmented and Dispersed by Nuclear Subsurface Explosions," *Journal of the Astronautical Sciences*, In Press, 2012.
- [5] B. Kaplinger, B. Wie, D. Dearborn, "Nuclear fragmentation/dispersion modeling and simulation of hazardous near-Earth objects," *Acta Astronautica*, In Press, 2012, <http://dx.doi.org/10.1016/j.actaastro.2012.10.013>.
- [6] A. Pitz, B. Kaplinger, G. Vardaxis, T. Winkler, and B. Wie, "Conceptual Design of a Hypervelocity Asteroid Intercept Vehicle and Its Flight Validation Mission," *AIAA/AAS Astrodynamics Specialist Conference*, Minneapolis, Aug 13-16, 2012.
- [7] *Effects of Nuclear Earth-Penetrator and Other Weapons*, National Research Council, 2005.
- [8] S. Wagner, and B. Wie, "Analysis and Design of Fictive Post-2029 Apophis Intercept Mission for Nuclear Disruption," AIAA-2010-8375, *AIAA/AAS Astrodynamics Specialists Conference*, Toronto, Ontario, Canada, August 2-5, 2010.
- [9] B.D. Kaplinger, and B. Wie, "Comparison of Fragmentation/Dispersion Models for Asteroid Nuclear Disruption Mission Design," AAS-11-403, *AAS/AIAA Astrodynamics Specialist Conference*, Girdwood, AK, July 31- August 4, 2011.
- [10] D.B. Kirk, W.W. Hwu, *Programming Massively Parallel Processors*, Morgan Kaufmann, Burlington, 2010.
- [11] J.M. Owen, J.V. Villumsen, P.R. Shapiro, and H. Martel, "Adaptive Smoothed Particle Hydrodynamics: Methodology. II," *The Astrophysical Journal Supplement Series*, 116:155209, June 1998.
- [12] G.R. Liu, and M.B. Liu, *Smoothed Particle Hydrodynamics: A Meshfree Particle Method*, World Scientific Publishing, Singapore, 2003.
- [13] D.S. Balsara, "von Neumann stability analysis of smoothed particle hydrodynamics- suggestions for optimal algorithms," *Journal of Computational Physics*, 121:357-372, 1995.
- [14] Benz, W., and Asphaug, E., "Simulations of Brittle Solids using Smooth Particle Hydrodynamics," *Computer Physics Communications*, vol. 87, pp. 253-265, 1995.
- [15] S. LeGrand, "Broad-Phase Collision Detection with CUDA," *GPU Gems 3*, ed. H. Nguyen, Addison-Wesley, 2007.

- [16] B. Kaplinger, and B. Wie, “High-Performance Computing for Optimal Disruption of Hazardous NEOs,” *AIAA/AAS Astrodynamics Specialist Conference*, Minneapolis, MN, Aug 13-16, 2012.
- [17] J.E. Lennard-Jones, “On the Determination of Molecular Fields,” *Proceedings of the Royal Society of London A*, 106 (738):463-477, 1924.
- [18] Curtis, H.D., *Orbital Mechanics for Engineering Students*, Elsevier Aerospace Engineering Series, Oxford, UK, 2006.
- [19] Vallado, D.A., *Fundamentals of Astrodynamics and Applications*, Third Edition, Microcosm Press, Hawthorne, CA, 2007.
- [20] Kaplinger, B., and Wie, B., “Optimized GPU Simulation of a Disrupted Near-Earth Object Including Self-Gravity,” AAS-11-266, *21st AAS/AIAA Spaceflight Mechanics Meeting*, New Orleans, LA, February 13-17, 2011.
- [21] Margot, J.L., Nolan, M.C., Benner, L.A.M., Ostro, S.J., Jurgens, R.F., Giorgini, J.D., Slade, M.A., Campbell, D.B., “Binary Asteroids in the Near-Earth Object Population,” *Science*, 296, 2002.
- [22] Michel, P., “Physical Properties of Near-Earth Objects that Inform Mitigation,” *2nd IAA Planetary Defense Conference*, Bucharest, Romania, May 9-12, 2011.

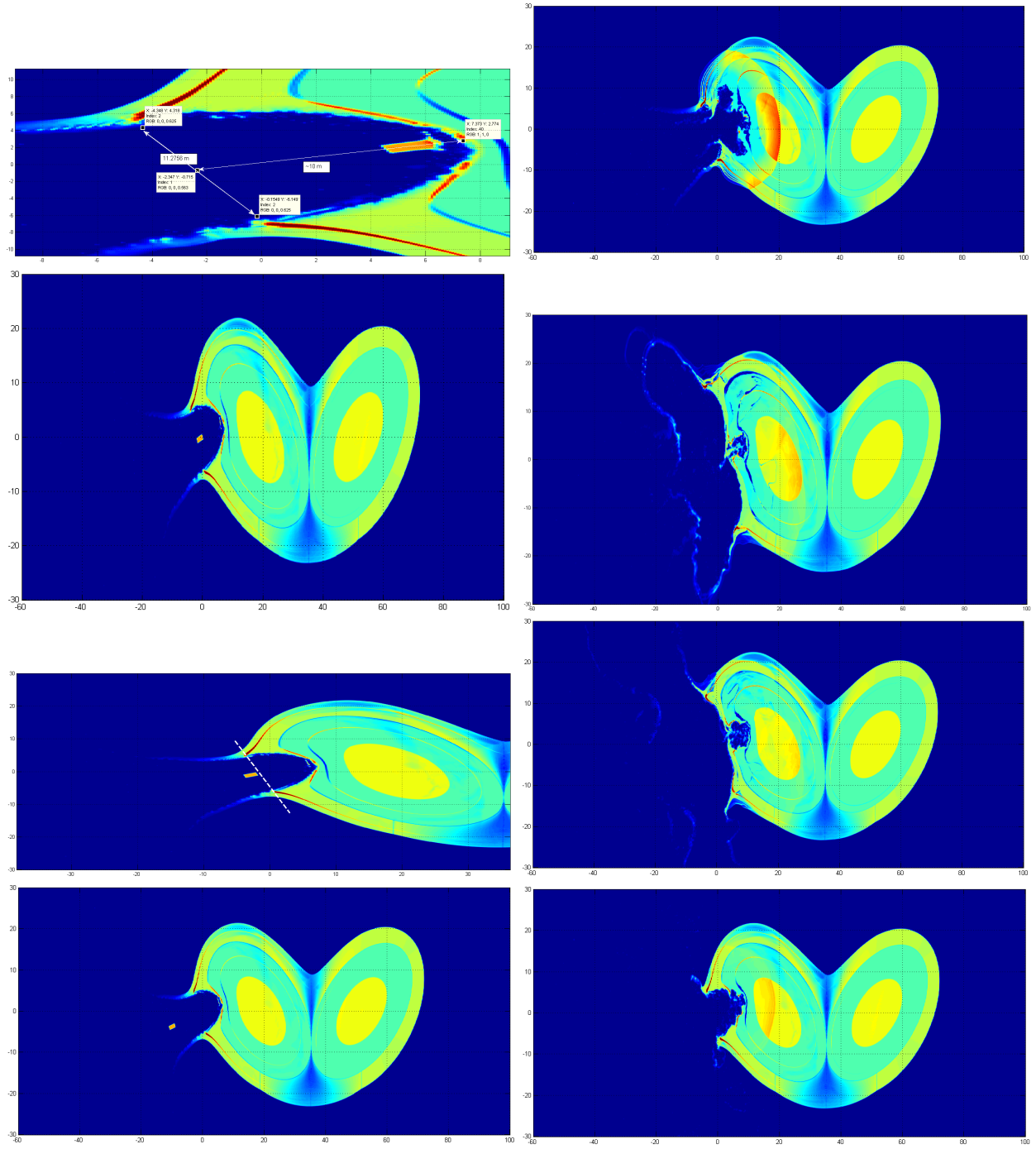


Figure 14: Disruption Behavior for Timing Test Points 1, 2, 3, and 4.

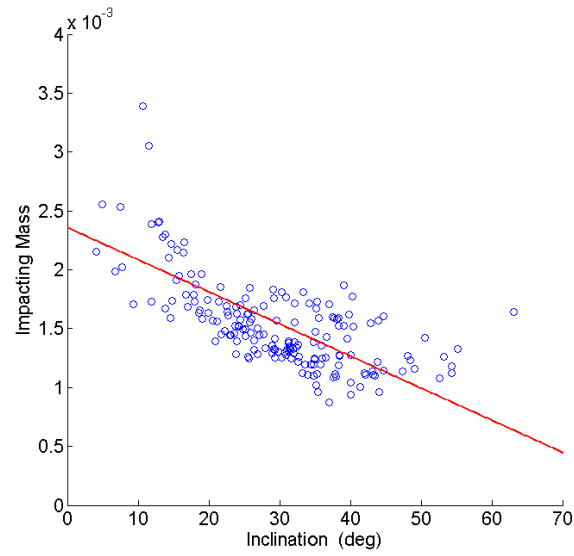


Figure 15: Impacting Mass for Subsurface Explosion on Orbits with Varying Inclination.

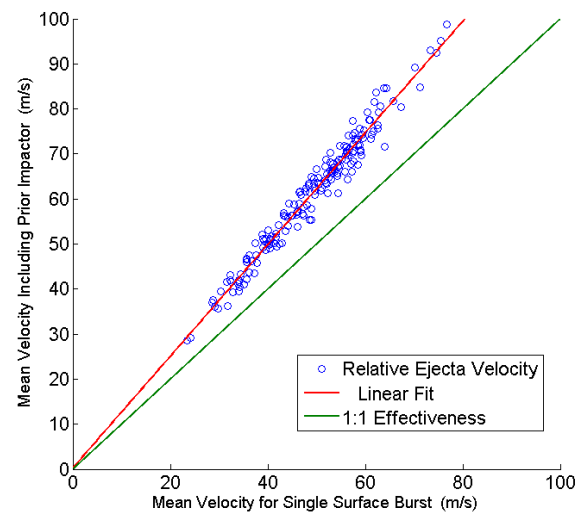


Figure 16: Mean Ejecta Velocity for Single and Double Impactor Cases.

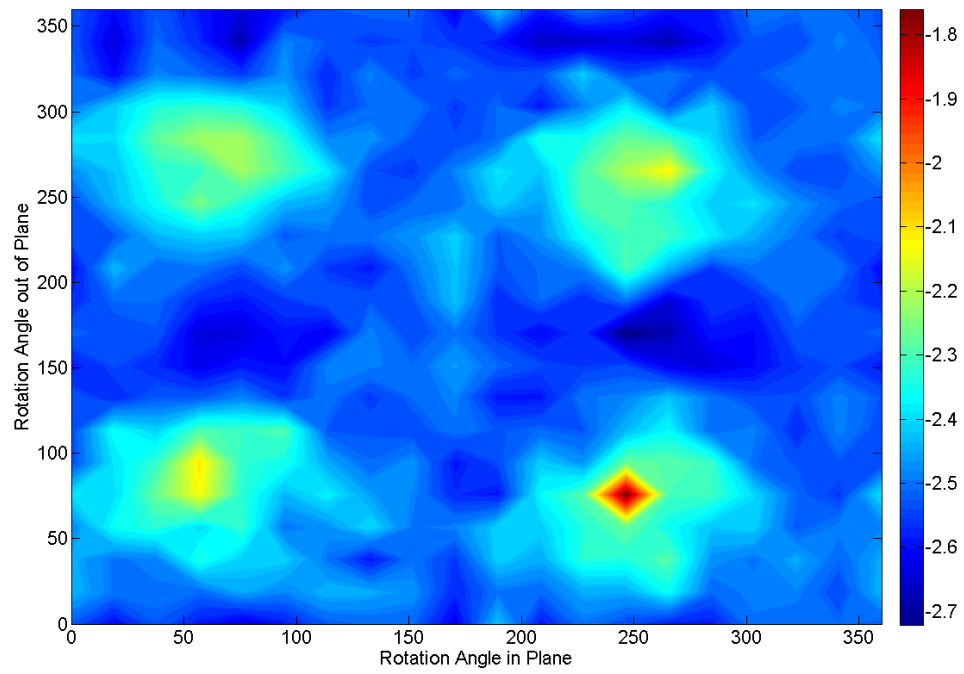


Figure 17: Cost Function Contours for Sample Mission Approach Asymptotes.